International Journal of Biological Macromolecules 267 (2024) 131392

Contents lists available at ScienceDirect

International Journal of Biological Macromolecules

journal homepage: www.elsevier.com/locate/ijbiomac

SARS-CoV-2 M^{pro} oligomerization as a potential target for therapy

Kinga Lis [a,b], Jacek Plewka [a], Filipe Menezes [c], Ewa Bielecka [d], Yuliya Chykunova [a,e], Katarzyna Pustelny [f], Stephan Niebling [g,h], Angelica Struve Garcia [g,h], Maria Garcia-Alai [g,h], Grzegorz M. Popowicz [c], Anna Czarna [f,*], Tomasz Kantyka [d,*], Krzysztof Pyrc [a,*]

[a] Jagiellonian University, Malopolska Centre of Biotechnology, Virogenetics, Laboratory of Virology, Gronostajowa 7a, 30–387 Cracow, Poland
[b] Faculty of Chemical Engineering and Technology, Cracow University of Technology, Warszawska 24,31-155 Cracow, Poland
[c] Helmholtz Munich, Molecular Targets and Therapeutics Center, Institute of Structural Biology, Ingolstädter Landstr. 1, 85764 Neuherberg, Germany
[d] Jagiellonian University, Malopolska Centre of Biotechnology, Laboratory of Proteolysis and Post-translational Modification of Proteins, Gronostajowa 7a, 30–387 Cracow, Poland
[e] Jagiellonian University, Faculty of Biochemistry, Biophysics and Biotechnology, Microbiology Department, Gronostajowa 7, 30-387, Cracow, Poland
[f] Jagiellonian University, Malopolska Centre of Biotechnology, Gronostajowa 7a, 30–387 Cracow, Poland
[g] European Molecular Biology Laboratory, EMBL Hamburg, Notkestrasse 85, Hamburg, Germany
[h] Centre for Structural Systems Biology (CSSB), Hamburg, Germany

ARTICLE INFO

Keywords:
M^{pro}
Dimerization
SARS-CoV-2

ABSTRACT

The main protease (M^{pro}) of SARS-CoV-2 is critical in the virus's replication cycle, facilitating the maturation of polyproteins into functional units. Due to its conservation across taxa, M^{pro} is a promising target for broad-spectrum antiviral drugs. Targeting M^{pro} with small molecule inhibitors, such as nirmatrelvir combined with ritonavir (Paxlovid™), which the FDA has approved for post-exposure treatment and prophylaxis, can effectively interrupt the replication process of the virus. A key aspect of M^{pro}'s function is its ability to form a functional dimer. However, the mechanics of dimerization and its influence on proteolytic activity remain less understood. In this study, we utilized biochemical, structural, and molecular modelling approaches to explore M^{pro} dimerization. We evaluated critical residues, specifically Arg4 and Arg298, that are essential for dimerization. Our results show that changes in the oligomerization state of M^{pro} directly affect its enzymatic activity and dimerization propensity. We discovered a synergistic relationship influencing dimer formation, involving both intra- and intermolecular interactions. These findings highlight the potential for developing allosteric inhibitors targeting M^{pro}, offering promising new directions for therapeutic strategies.

1. Introduction

The SARS-CoV-2 pandemic emerged at the end of 2019. Within the initial two-year span, it claimed approximately 20 million lives, as estimated from available data [1]. As the virus responsible for COVID-19 spread globally, it swiftly ascended to become one of the most pressing challenges to global public health, inflicting severe repercussions on human well-being, economies, and societal structures worldwide. Despite continuous efforts and effective vaccines, the virus continues to pose a substantial risk to individuals, necessitating the development and distribution of effective treatments in the years ahead. Further, it is safe to assume that, considering the propensity of coronaviruses to cross species boundaries, devising effective therapeutic strategies is of paramount importance to minimize the future impact.

SARS-CoV-2 is an enveloped, positive-sense, single-stranded RNA virus that belongs to the betacoronavirus genus within the *Coronaviridae* family. Its relatively large genome, spanning nearly 30,000 nucleotides, encodes four structural proteins – spike (S), envelope (E), membrane (M), and nucleocapsid (N) - along with 16 non-structural proteins (nsp) [2,3]. Among the latter, M^{pro}, also known as 3-chymotrypsin-like proteases ($3CL^{pro}$) or nsp5, is one of the most important molecular targets for COVID-19 therapy. M^{pro} serves as SARS-CoV-2's main protease, initially excising itself and subsequently maturing the viral polyprotein into functional proteins. Enzymatic cleavage of the SARS-CoV-2 polyprotein by M^{pro} occurs at 11 recognition sites, within the consensus sequence Q↓(S/A/G/N) at P1 and P1` positions, with the conserved glutamine at position P1. This process is a fundamental step, that facilitates virus replication post-cell entry, and its inhibition abrogates the

* Corresponding authors.
E-mail addresses: anna1.czarna@uj.edu.pl (A. Czarna), tomasz.kantyka@uj.edu.pl (T. Kantyka), k.a.pyrc@uj.edu.pl (K. Pyrc).

https://doi.org/10.1016/j.ijbiomac.2024.131392
Received 5 March 2024; Received in revised form 2 April 2024; Accepted 3 April 2024
Available online 4 April 2024

infection [4,5].

A monomeric M^{pro} consists of three domains, encompassing residues 8 to 101 (I), 102 to 184 (II) and 201 to 303 (III). Domains I and II are organised as a six- and five-stranded antiparallel β-barrels, whereas domain III (C-domain), has five α-helices forming a globular cluster. Residues 185 to 200 form a long loop, which connects domain II with domain III [6]. A substrate-binding pocket in active M^{pro} is divided into five main regions: S1, S2, S3, S4 and S5 corresponding to P1, P2, P3, P4, and P5 substrate-binding positions, respectively [3,7]. A properly formed pocket plays a vital role in enzymatic catalysis, as it is responsible for substrate recognition, specificity, and binding stability [8,9]. The M^{pro} active site, laying in the cleft between domains I and II, features a His41 and Cys145 dyad [3,10–12]. M^{pro} exerts its proteolytic activity only as a homodimer [2] and dimerization is mediated by the binding interface. The C-domain in M^{pro} is atypical for cysteine proteases and exists only in *Nidovirales*, including coronaviruses. It is referred to as the "extra helix domain" and is essential for proper dimerization by enabling the formation of a fully functional enzyme [3,13,14]. Together with other regions of the protein, including the N-finger (Ser1-Ala7), A' helix (Ser10-Gly15), as well as the S1 substrate-binding pocket residues (Phe140, Gly143, Ser144, Cys145, His163, Glu166, His172) [3], forms the dimer interface [6,15], that stabilizes and controls the dimer formation. As dimerization is indispensable for M^{pro} activity, these residues may serve as potential targets for new antiviral drugs, designed to disturb the active dimer formation. The residues Arg4, Ser139, Glu 290, or Arg298 are suggested to be of importance for homodimer formation and stabilization, with the special role of a salt bridge formed between Arg4 and Glu290, and inter- and intra-protomer interactions of Arg298 with Ser123 and Met6, respectively [6,16]. However, despite SARS-CoV M^{pro} being one of the most intensively studied proteins, there are many inconsistencies in the literature about the role of N-terminus and C-domain residues regarding dimer formation and proteolytic activity.

M^{pro} is among the molecular targets with proven clinical relevance for coronavirus therapy. Many attempts have been made to investigate potential inhibitors, including drug repurposing, small molecule inhibitors or the development of novel compounds capable of inhibiting protease activity [17,18]. Nirmatrelvir is a clinically approved and highly effective protease inhibitor. However, drug resistance has been already reported [19–22]. This necessitates the identification of novel molecular targets, which may be used in a combined therapy or as alternative. Here we propose a novel site on M^{pro}, which is located beyond the catalytic pocket and may be targeted to hamper the enzyme's dimerization. Such a strategy could pave the way for the development of innovative therapeutic interventions that would not be affected by the cross-resistance with existing protease inhibitors. Since M^{pro} is a relatively conserved protein, and majority of so-far known SARS-CoV-2 M^{pro} rare mutations (P132H, K90R, L89F, P108S, A260V or K88R) occur at sites other than the dimer interface, M^{pro}'s dimer interface becomes an even more convenient molecular target for the therapy [23–26].

This study analysed the role of six different combinations of SARS-CoV-2 M^{pro} Arg4 and Arg298 mutations, targeting two of the most prominent inter- and intra-monomer interactions and affecting dimer formation. A range of techniques was used to evaluate the oligomerization state of different variants of M^{pro}, including biochemistry studies, and biophysical analyses, together with structural, molecular dynamics, and quantum mechanical analysis. M^{pro} dimerization was characterized by determining K_D values and following the 'in solution/close-to-native state' dimerization dynamics by means of a novel mass photometry technique. The importance of the analysed residues on the enzyme's activity and dimerization was established. The findings illuminate the role of allosteric sites and the potential for devising novel molecular targets for anticoronaviral therapies. Given the high level of conservation of the M^{pro} protease between coronaviruses, inhibiting dimer formation can serve as a new universal strategy for designing antiviral agents not only for SARS-CoV-2 M^{pro}, but also for related viruses.

2. Materials and methods

2.1. Enzymatic assays

Enzymatic activity assays of all M^{pro} mutants and the WT form were performed on 96-well black assay plates using synthetic peptidic M^{pro} substrate Ac-VKLQ-(AMC) in assay buffer (20 mM TRIS pH 7.3, 150 mM NaCl, 1 mM EDTA, 2 mM DTT, 0,05 % Tween). Molar specific activity (MSA) was calculated as the activity of the enzyme divided by the unit of concentration. Effective activity (EA) of enzyme was assessed as molar specific activity divided by the apparent K_D (K_D^{app}), whereas K_D^{app} values were determined with the built-in one-site specific binding model using GraphPadPrism.

Measurements were carried out on SpectraMax Gemini EM Microplate Reader for 1 h with 20s intervals at 37 °C while shaking. Excitation and emission wavelengths were 350 nm and 460 nm, respectively. All experiments were carried out in triplicates, and were also repeated on different batches of proteins. All M^{pro} variants were measured according to the same protocol, different only in the range of tested concentrations, as presented in Table 1.

2.2. MicroScale thermophoresis

Proteins were labelled using the Monolith Protein Labeling Kit RED-NHS 2nd Generation (Nanotemper), according to manufacturer's guidelines. As a next step, the labelled proteins were diluted in PBS with 0.05 % Tween-20 up to the desired concentration, mixed with non-labelled proteins and incubated at RT for 30 min. Measurements were carried out in dedicated standard capillaries on Monolith NT.115 with the pico detector using 80 % excitation power and high MST power or Dianthus equipped with the pico detector using the dedicated plates in two independent dilution series. The results were averaged and fitted in Mathematica 12 with following equation:

$$FB = \frac{[AB]}{[B]} = \frac{[A] + [B] + K_D - \sqrt{([A] + [B] + K_d)^2 - 4[AB]}}{2[B]}$$

where:

FB – fraction bound
[A] – concentration of unlabeled titrated partner
[B] – concentration of fluorescent labelled partner that is fixed
[AB] – concentration of bound complex of A and B
K_D – equilibrium dissociation constant

2.3. Mass-photometry analyses

All mass photometry measurements were acquired on a commercial Refeyn OneMP mass photometer using the software Refeyn Acquire MP (version: 2022 R1). All M^{pro} variants (concentrations ranging from 2 to 10 mg/ml) were spin down for 20 min at 13.2×10^3 rpm (16×10^3 RCF). The buffer consisting of 50 mM TRIS pH 8, 150 mM NaCl and 1 mM TCEP was filtered with a 30 kDa cutoff filter (Amicon Ultra 0.5 ml 30 K)

Table 1
Range of tested M^{pro} concentrations for enzymatic activity studies and apparent K_D determination.

M^{pro} variant	Protein concentration range [nM]
M^{pro} WT	5–2000
M^{pro} R4A	
M^{pro} R4Q	
M^{pro} R298A	100–10,000
M^{pro} R298Q	500–20,000
M^{pro} R4A R298Q	1000–15,000
M^{pro} R4Q R298Q	2000–40,000

Table 2
Composition of crystallization buffers for all analysed M^{pro} variants.

M^{pro} variant	Crystallization conditions
M^{pro} WT	20 % Polyethylene glycol monomethyl ether 5.000, 200 mM Potassium formate
M^{pro} R4A	20 % Polyethylene glycol monomethyl ether 5.000, 200 mM Potassium formate
M^{pro} R4Q	25 % PEG 3350, 200 mM magnesium chloride hexahydrate, 0.1 M Bis-Tris pH 5.5
M^{pro} R298A	20 % PEG 3350, 0.18 mM benzamidine hydrochloride, 200 mM potassium formate
M^{pro} R298Q	20 % PEG 3350, 0.1 mM benzamidine hydrochloride, 200 mM potassium formate
M^{pro} R4A R298A	20 % PEG 3350, 0.12 mM benzamidine hydrochloride, 200 mM potassium formate
M^{pro} R4Q R298Q	20 % PEG 3350, 0.1 mM benzamidine hydrochloride, 200 mM potassium formate

prior to usage as described previously [27]. Predilutions of the M^{pro} proteins were prepared at concentrations of 1 μM, 500 nM, 100 nM, 40 nM and 20 nM by a serial dilution. 1 μl of these pre-dilutions were then added to 18 μl of the buffer on the cleaned microscope slide (Thorlabs High Precision Microscope Cover Glasses 25 × 50 mm, 170 μM, No. 1.5H). The cleaning procedure is described elsewhere [27]. After thorough mixing the measurement was started. For all mass photometry measurements the 'regular' image size was used. The mass photometer was calibrated using three proteins at 66, 146 and 480 kDa of a commercial protein ladder (Invitrogen Native Mark Unstained Protein Standard). Details regarding the calibration can be found in [27]. Events were fitted using the software Refeyn Discover MP (version: 2022 R1) and exported as .h5 files for further analysis. For further data analysis (histogram creation and gaussian fitting), the eSPC module [28] PhotoMol was used. PhotoMol is available at https://spc.embl-hamburg.de.

2.4. Crystallization and data collection

Purified proteins were concentrated (to about 10–11 mg/ml) and crystallization was performed at RT with the use of the sitting drop vapour diffusion method, with the ratio of protein to mother liquor as 0.3 μl:0.3 μl. Crystallization conditions for each of protein are presented in Table 2.

The crystals were cryoprotected in 30 % ethylene glycol in the mother liquor and snap-frozen in liquid nitrogen. The diffraction data were collected at P11 at PETRA III beamline operated by the DESY photon facility, BL14.1 beamline at BESSY and ID14 at ESRF. The data were indexed, integrated, and scaled using XDS and Aimless [29]. The initial phases were obtained by the molecular replacement protocol using Phaser software [30].The model was built into the electron density using Coot [31] and subsequent refinement was performed using Refmac or PDB-REDO server [32].

2.5. Computational study

The dimers of M^{pro} and its several mutants were constructed with Chimera [33] using the crystal structure of the mutant R298A as a template. Dynamical simulations were run using GROMACS [34] together with the CHARMM36 [35] force field. Explicit water solvation was modelled with the CHARMM-modified TIP3P water [36]. Productive simulations were conducted in the NPT ensemble following standard protocols [37]. Temperature and density were controlled between equilibration stages. Productive simulations were also controlled on temperature and density to ensure the stability of the trace. The gCorrelation plots [38] were obtained from the whole simulation without applying any cutoff, and on the last 200 ns of simulation. Quantum mechanical calculations were run using ULYSSES [39], our in-house quantum chemical package. The Hamiltonian of choice was GFN2-xTB [40] with ALPB [41] implicit solvation. Note that for the quantum mechanical evaluation all explicit waters were excluded, leaving only the implicit solvation. Cutting and isolation of M^{pro} subregions was accomplished with Chimera from the dynamical traces, and figures prepared with ChimeraX [42,43].

3. Results

3.1. Proteins

The SARS-CoV-2 WT M^{pro} (wild type, residues 3264–3569) gene was synthesized by GenScript and subcloned into pETM30 vector (Supplementary Material, 1.1.). Site-directed mutagenesis was used to obtain six mutants of SARS-CoV-2 M^{pro}: R4A, R4Q, R298A, R298Q, R4A R298A, R4Q R298Q, where positively charged Arg4 and Arg298 were replaced either with the smaller, neutral alanine, or with a glutamine, uncharged, yet of similar side chain length, and offering the possibility for π-stacking. The purity of obtained M^{pro} variants (Supplementary Material, 1.2.) was assessed using SDS-PAGE (Fig. S1) and size exclusion chromatography (SEC) (Supplementary Material, 1.3., Fig. S2). In its monomeric state, SARS-CoV-2 M^{pro} has a calculated MW of 32 kDa. Analysis of the SEC profiles with the MW standards reveals that M^{pro} WT, R4A, and R4Q eluted as dimers as indicated by their elution peak at *ca.* 10 ml (~64 kDa). On the other hand, M^{pro} R298A, M^{pro} R298Q, M^{pro} R4A R298A, and M^{pro} R4Q R298Q variants eluted in their monomeric forms with elution peaks at EV *ca.* 11.5 ml (~32 kDa) under given conditions (protein concentration 1 mg/ml, 20 mM Tris pH 7.4, 150 mM NaCl, 2 mM β-mercaptoethanol).

3.2. Determination of the oligomeric state of M^{pro} variants

For a more in-depth analysis of M^{pro} variants in solution, which allows studying their behavior under near-natural conditions, mass photometry (MP) was employed. MP facilitates the determination of the variation in the apparent molecular masses of M^{pro} variants, enabling unequivocal discrimination between the monomeric and multimeric forms. This technique utilizes interference reflection microscopy and interferometric scattering microscopy to quantify the amount of light scattered by a single molecule adsorbed on a glass surface; the molecular mass of the measured protein can be calculated directly from the interferometric contrast.

For each sample, the highest and the lowest applicable concentrations were determined, ensuring reliable measurements. Samples in the buffer spiked with 2 M urea were measured (25 nM each), allowing assessment of the MWs of M^{pro} monomers, serving as negative controls.

The MP results (Fig. 1) indicate that the dominant form of WT M^{pro} is the dimer, even at concentrations as low as 1 nM. The dimerization equilibrium of the M^{pro} R4A mutant, however, is slightly shifted towards the monomer form. A further decrease in effective dimer formation was observed for M^{pro} R4Q, even at concentrations of 25 nM, a significant amount of monomer is observed (42 %). As dimerization is dependent on protein concentration, it is presumed that a dimer/monomer equilibrium was achieved at least for the WT, R4Q, and R4A M^{pro} variants. The monomer-dimer equilibrium in solution at given concentrations was fitted to a normalized Hill equation to determine the dimerization constant (Fig. S3). For these M^{pro} variants, dimerization constants were in the low nanomolar range (0.26 nM for WT M^{pro}, and 0.59 nM for R4Q and R4A M^{pro} variants) and in fair agreement with the apparent constants determined by the activity study (see subsequent paragraphs).

The mass distribution and consequently the oligomerization characteristics of the remaining M^{pro} mutants (R298Q, R298A, double

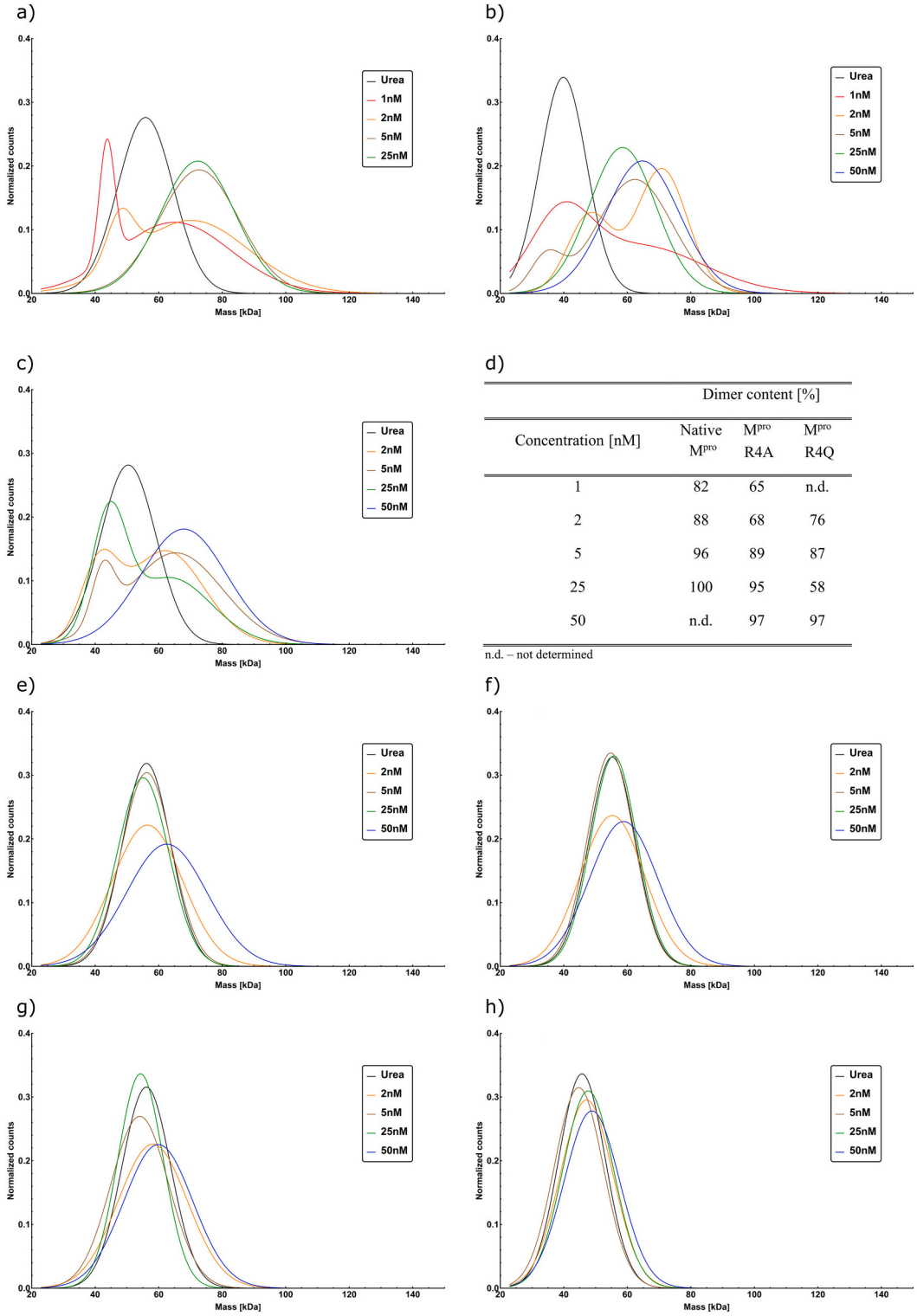

d)

Concentration [nM]	Dimer content [%]		
	Native M^{pro}	M^{pro} R4A	M^{pro} R4Q
1	82	65	n.d.
2	88	68	76
5	96	89	87
25	100	95	58
50	n.d.	97	97

n.d. – not determined

Fig. 1. Molecular mass distribution for a) WT M^{pro}, b) M^{pro} R4A, c) M^{pro} R4Q, e) M^{pro} R298A, f) M^{pro} R298Q, g) M^{pro} R4A R298A, h) M^{pro} R4Q R298Q at various concentrations using mass photometry approach. The molecular weight depicted as normalized gaussian distributions (fitted from the generated mass histograms) of probabilities of particular masses. The urea sample denotes the M^{pro} variant at 25 nM concentration in a buffer with 2 M urea serving as a negative control of the M^{pro} monomer mass distribution profile. d) The table in the upper panel presents the percentage content of dimer in the analysed samples for M^{pro} WT, M^{pro} R4A and M^{pro} R4Q. For the remaining variants, only the monomer was observed across the entire range of tested concentrations.

mutants R4Q R298Q, and R4A R298A) were not affected by increasing protein concentrations and were similar to the negative controls denatured in the 2 M urea. This indicates a predominantly monomeric state for those variants, observed for concentrations within reach of mass photometry (50 nM). Again, this observation is in fair agreement with the apparent K_D determined by activity assays.

It should be noted that the MW estimation for the monomeric M^{pro} is of low precision, as the M^{pro} monomer size is near the lower detection limit of the mass photometer [44]. Consequently, the recorded histogram is not symmetrical on the lower mass side, the fitted Gaussian peak

for monomers is displaced towards the higher molecular weight range (Fig. S4). However, the relative positions of M^{pro} monomers were unambiguously determined, based on the negative control measurements in the presence of 2 M urea.

To further evaluate the interactions of M^{pro} monomers and to assess the actual K_D of dimerization, MicroScale Thermophoresis (MST) was employed. Labelled proteins were mixed with unlabelled ones and the resulting signals were fitted with a 1:1 binding mode equation.

K_D was successfully determined for WT M^{pro}, as well as all single mutants (Table S2, Fig. S5). The lowest K_D value was observed for WT M^{pro}, reaching 1.3 nM, with slightly higher values for M^{pro} R4A: 5.7 nM and M^{pro} R4Q: 5.8 nM. In the case of R298A and R298Q variants, K_D values reached 158 nM and 389.4 nM, respectively. Accurate dimerization constants could not be determined for the double M^{pro} mutants R4A R298A and R4Q R298Q within the achievable protein concentration range - however, the estimated K_D in both cases exceeded 1000 nM. The experimental setup posed challenges due to numerous potential binding scenarios, involving interactions not only between the labelled protein and the measured unlabelled one, but also between unlabelled proteins, contributing to relatively high error bars in the measurement points.

3.3. Characteristics of an enzymatic activity of M^{pro} and its variants

To assess whether the oligomerization state of SARS-CoV-2 M^{pro} affects its proteolytic activity, M^{pro} variants were subjected to enzymatic assays to determine their molar specific activities (MSA), reflecting their efficiency in substrate processing. The specific activity provides information about the enzyme's activity per unit of concentration, directly translating into efficacy. The fitted curve enables the determination of the apparent K_D, while differences in the molar specific activity indicate impairments in substrate processing between compared variants of M^{pro} proteases.

In the case of WT M^{pro}, as well as M^{pro} R4A and M^{pro} R4Q mutants, the MSA values are similar (ranging from $4.6{\cdot}10^{-3}$ to $8.6{\cdot}10^{-3}$ RFU/s/nM). In contrast, the MSA for the M^{pro} R298A and M^{pro} R298Q mutants is reduced 2- to 3-fold compared to WT M^{pro}. The double mutants M^{pro} R4A R298A and M^{pro} R4Q R298Q show a significant loss in their MSA compared to the WT. In particular, the latter mutant exhibits almost a 12-fold decrease in MSA, reaching only $3.9{\cdot}10^{-4}$ RFU/s/nM. MSA measurements clearly demonstrate, that the highest effective activity is observed for WT and Arg4 mutants, whereas in the case of R298 and double mutants, the efficiency of their catalytic machinery is significantly diminished.

To characterize the dimer formation of the analysed M^{pro} variants, the apparent K_D constants (K_D^{app}) were determined. The lowest K_D^{app} value (6.6 nM) was observed for the WT M^{pro}. Two highly active Arg4 mutants, both R4A and R4Q, are characterized by slightly higher K_D^{app} values when compared to WT M^{pro}, 22.3 nM and 19.1 nM, respectively. However, a significantly higher K_D^{app} is observed for the R298A and R298Q M^{pro} variants, reaching $11.6{\cdot}10^{2}$ nM and $36.0{\cdot}10^{2}$ nM, respectively. These values are even higher for the double mutants R4A R298A and R4Q R298Q, reaching $43.7{\cdot}10^{2}$ nM and $20.94{\cdot}10^{3}$ nM, respectively. Taken together, the K_D^{app} values for WT, R4A and R4Q M^{pro} align with those commonly reported for active, dimeric forms of M^{pro}. In the case of the Arg298 and the double mutants, the K_D^{app} are significantly higher, indicating the disruption of the dimerization process in comparison to the WT.

The combination of K_D^{app} and MSA values allowed the characterization of all M^{pro} variants also by the resulting effective activity (EA), calculated as MSA/K_D^{app}, which denotes the catalytic activity against a measure of the propensity for dimer formation. The analysis revealed that WT M^{pro} features the highest EA, whereas the other variants exhibit lower effectiveness, with only 0.046 % and 0.003 % for R4A R298A and R4Q R298Q, respectively. All the described data are presented on Fig. 2 and summarized in Table 3.

3.4. Protein structure analyses and computational studies

3.4.1. Crystallographic analysis

All M^{pro} variants were successfully crystallized under the conditions summarized in the Materials and Methods section. All crystals belong to a monoclinic system, differing in terms of lattice centering: primitive for M^{pro} R298A (P121), base-centered for M^{pro} R298Q, M^{pro} R4A, and M^{pro} R4Q (C121) and body-centered for M^{pro} WT (I121) (Table S3). For each crystal analysed, except for M^{pro} R298A, there is only a single chain (monomer) in the crystal asymmetric unit (ASU), which can be easily transformed into the crystallographic dimer by symmetry expansion. In the case of M^{pro} R298A, there are two chains in the ASU. In a comprehensive analysis of all studied SARS-CoV-2 M^{pro} variants (data not shown), the tertiary structure of the secondary fold exhibits pronounced conservation. Relative to the WT M^{pro} conformation, the RMSD (Root Mean Square Deviation) values of the Cα atoms consistently indicate a high structural similarity of the studied variants.

3.4.2. Molecular dynamics simulations (MD)

To understand the molecular mechanism for the experimental observations, Molecular Dynamics (MD) simulations in explicit water were run for WT M^{pro} and its 6 mutants. The starting structures for the dimers were constructed from the respective crystallographic data. Simulations were run for 500 ns each. Fig. 3 shows an overlay of the dynamical traces for WT M^{pro} and the R4Q R298Q mutant. Other overlays are given in the Supplementary Material (Figs. S6–S10).

The overlays of WT M^{pro} and mutant dynamical traces present pronounced differences (Fig. 3, panel a) and b)), which are reflected in the RMSDs and RMSFs (Root Mean Square Fluctuation) of the simulation (Fig. 3, panel c)) and the respective associated statistics (Table S4). The simulations evidence that the WT M^{pro} dimer, after a short relaxation from the starting dimer structure, remains stable at an RMSD of about 2.3 Å. WT M^{pro} is the dimer exhibiting the highest stability and rigidity, seen over the average and the standard deviation of the RMSD. For the mutant dimers studied, RMSDs are significantly higher and more variable, what reflects an increase in conformational entropies. Similar conclusions may be drawn from the RMSF data.

3.4.3. Interactions between residues in M^{pro} dimers

To obtain an overview of the whole MD simulations and to extract information on the M^{pro} dimerization status, the gCorrelation method of Lange and Grubmueller was used [38]. Utilizing the principles of information theory, the mutual information between two residues throughout a simulation was assessed, discriminating potential correlations in both the motion and the interactions of residues within dimeric M^{pro} and its variants. The gCorrelation takes values between 0 for uncorrelated motion, and 1 for full correlation. The map of correlations for WT and R4QR298Q M^{pro} calculated over the Cαs of each residue is given in Fig. 4. The Supplementary Material contains also the gCorrelation plot for the R4AR298A double mutant (Fig. S11).

In the case of WT M^{pro}, there is a strong correlation for residues within domain III, and to a lesser extent in domains I and II. While domains I and II seem to correlate with each other, domain III acts independently. A prominent interaction between domains I and II, established between the main chains of Cys85 and Gly179 (interaction D in Fig. 4), was identified.

Specific points of contact also exist between the different M^{pro} monomers composing the dimer. Like the interaction between the domains I and II, these correspond to hydrogen bonds between main-chain atoms. The interaction between the Ser10 of the different M^{pro} molecules is an exception, as it is mediated through the side chains of the respective amino acids. The gCorrelation map presented in Fig. 4 shows no evidence of relevant inter- or even intra-monomer interactions involving Arg4 or Arg298, as the present gCorrelation map involves only Cαs and the side chains of arginines are flexible enough to dampen possible correlations. However, on the gCorrelation plot for WT M^{pro}

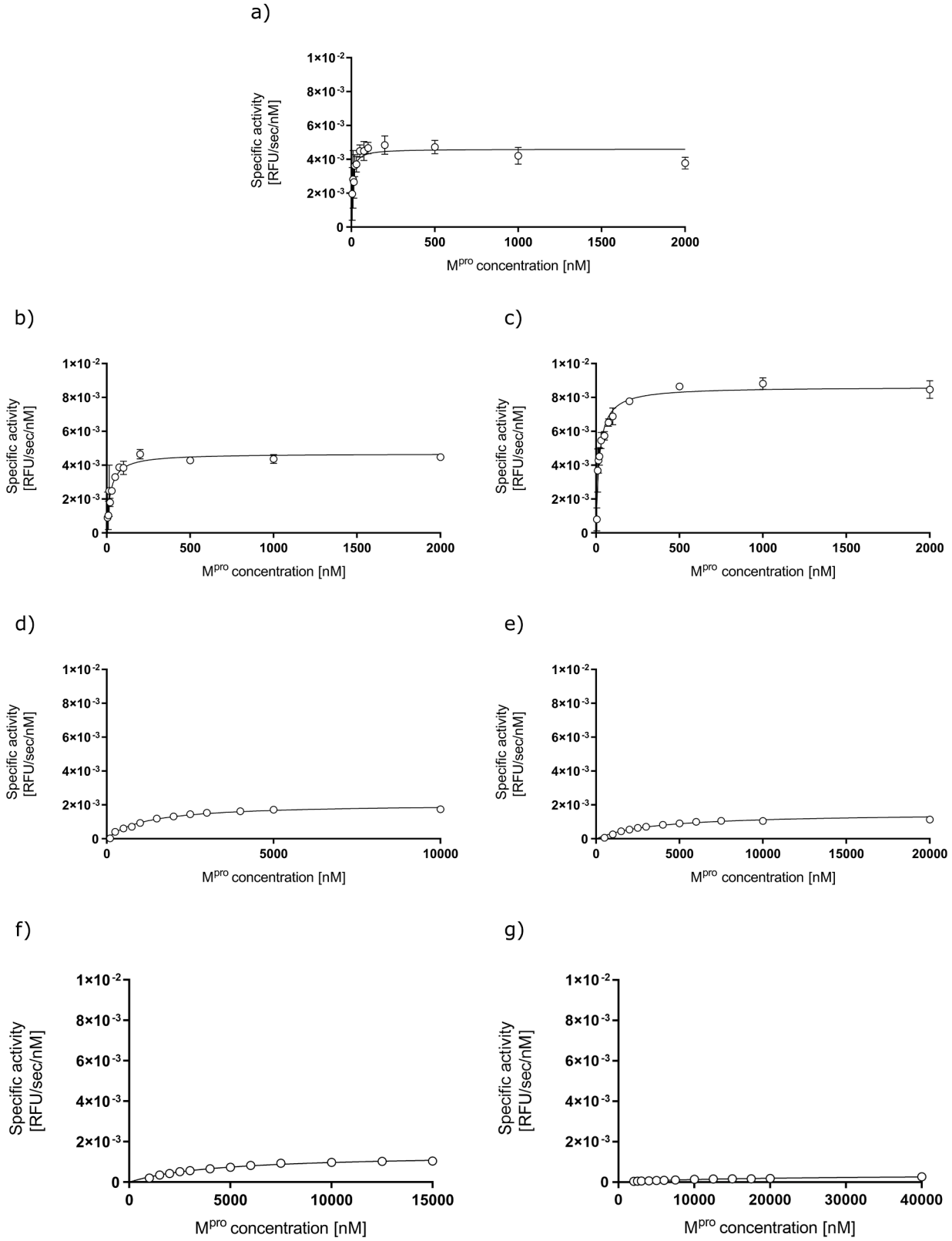

Fig. 2. Specific activity curves for a) WT M^{pro} protease and its mutants: b) M^{pro} R4A, c) M^{pro} R4Q, d) M^{pro} R298A, e) M^{pro} R298Q, f) M^{pro} R4A R298A, g) M^{pro} R4Q R298Q. The activity of different variants of M^{pro} was measured on the synthetic peptide substrate Ac-VKLQ-(AMC). The enzyme velocities at each concentration (RFU/s) were recalculated to specific activity (RFU/s/nM). The graphs represent the data from three independent experiments, each made in triplicates, and are presented as mean ± SEM.

Table 3
Summarized apparent K_Ds (K_D^{app}), molar specific activity (MSA), effective activity (EA), and % of activity for all tested M^{pro} variants. Data fitting for the estimation of the apparent K_D values was performed with a built-in one site-specific binding model using GraphPadPrism.

M^{pro} variant	K_D^{app} [nM]	MSA [RFU/s/nM]	EA [RFU/s] $\cdot 10^6$	% of activity
M^{pro} WT	6.6 ± 1.44	$4.6 \cdot 10^{-3} \pm 1.7 \cdot 10^{-4}$	699	100
M^{pro} R4A	22.3 ± 3.249	$4.7 \cdot 10^{-3} \pm 1.7 \cdot 10^{-4}$	210	30
M^{pro} R4Q	19.1 ± 1.458	$8.6 \cdot 10^{-3} \pm 1.5 \cdot 10^{-4}$	451	64
M^{pro} R298A	$11.6 \cdot 10^2 \pm 0.75 \cdot 10^2$	$2.1 \cdot 10^{-3} \pm 4.3 \cdot 10^{-5}$	1.78	0.254
M^{pro} R298Q	$36.0 \cdot 10^2 \pm 2.72 \cdot 10^2$	$1.5 \cdot 10^{-3} \pm 5.1 \cdot 10^{-5}$	0.42	0.061
M^{pro} R4A R298A	$43.7 \cdot 10^2 \pm 2.48 \cdot 10^2$	$1.4 \cdot 10^{-3} \pm 3.3 \cdot 10^{-5}$	0.32	0.046
M^{pro} R4Q R298Q	$20.94 \cdot 10^3 \pm 1.786 \cdot 10^3$	$3.9 \cdot 10^{-4} \pm 1.7 \cdot 10^{-5}$	0.02	0.003

side chain atoms, the interaction between Arg4 and Glu290 is observed as a local maximum of inter-residue correlation (Fig. S12). The gCorrelation matrix for the double R4Q R298Q mutant of M^{pro} (Fig. 4b)) is markedly different, with increased correlation in residue motion associated with all domains. For regions within each monomer, in particular the interactions between domains I and II, there is a marked increase in correlation; and for regions between different monomers there is a moderate increase in correlation. The gCorrelation plot for the mutant shows a significant degree of interdependence in the motion of the respective residues. This means that the natural oscillatory behavior of domain III, which in WT M^{pro} is fully independent of the rest of the protein, interferes and gets interference from the other two domains and the other monomer. This interpretation allows bridging the overlays of the dynamic traces with the results of the gCorrelation.

Taking all data together, the effect of any of the mutations on each domain can be understood as if each of the M^{pro} monomers is exhibiting a triple arhythmic behavior, one for each subdomain. Consequently, the gCorrelation plot also shows that the selected mutations affect the structure, rigidity, and internal order of each monomer of M^{pro}, therefore also impacting the dimer and its formation. This provides support for the entropic effect suggested in the previous section.

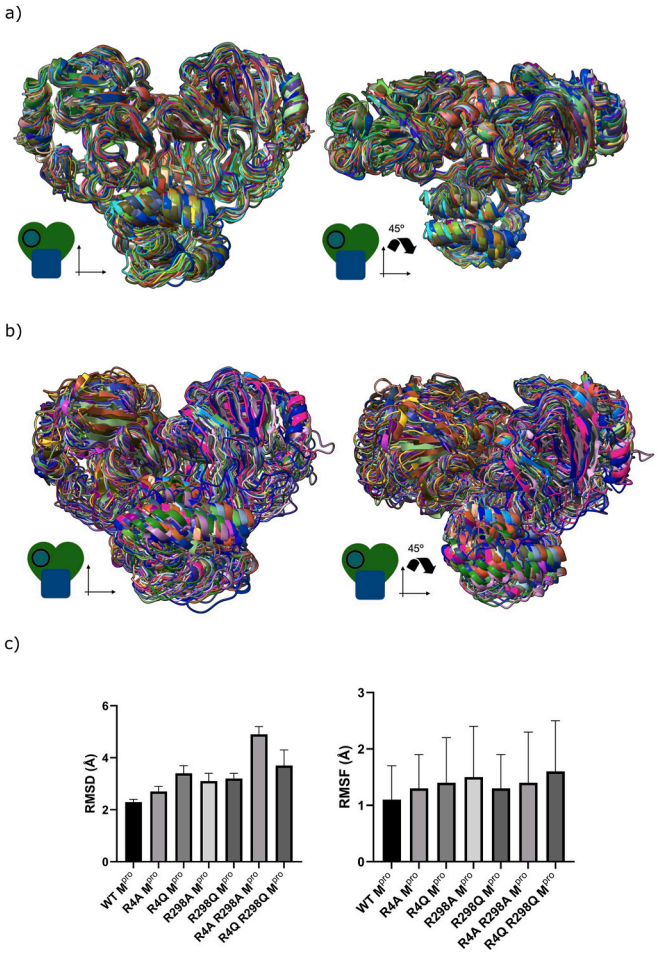

Fig. 3. Overlay of 500 ns of simulation time for a) M^{pro} WT and b) R4Q R298Q dimers with c) RMSD and RMSF statistic data. Structures collected and represented every 10 ns. RMSD statistics of each M^{pro} variant as a function of time with respect to the initial structures, RMSF calculated for one protomer of M^{pro} and each of its mutants for the last 200 ns of simulation. On the lower left corner of each Fig., a schematic representation of the molecule is given. The green heart-shaped component represents the dimerized domains I and II. The blue-square represents the C-domain and the circle indicates the catalytic domain of M^{pro}.

3.4.4. *Domain-specific interaction energies*

To obtain a better understanding of the impact of the mutations on the system's internal energetics, domain-specific interaction energies were calculated. Among others, a generic disposition and interaction mode for the intra-monomer interface between the N-finger and domain III of M^{pro} or the average binding energy between the N-finger (residues 1–7) and extended N-finger (residues 1–15) with domain III, together with additional data further describing intra-monomer interactions and statistical calculations can be found in Supplementary Materials (Figs. S13–S21, Tables S5, S6).

The average and lowest recorded binding energies take place for WT M^{pro}. All mutants show looser interactions, which reflects the loss of rigidity of the overall structure, and the decreased stability of the monomers in the dimer. When extending the residues included in the N-finger, a general decrease in interaction energies is observed. In the case of the R4AR298A mutant, interaction energies decrease by 1.6 kcal/mol with respect to the calculations including only the N-finger. The double R4QR298Q mutant registers a decrease of 2 kcal/mol, whereas WT M^{pro} stabilizes by almost 3.5 kcal/mol. Though far from the ideal structural configuration, the increased interaction between the side chains of Arg298 and Phe8 was registered, which potentially accounts for the observation. Irrespective of the nature of the interaction, the calculations reveal the non-negligible role of the extended N-finger domain for the stability of the monomers in the dimer.

The effect of mutations on the interaction energies between the extended N-finger and domain III belonging to different monomers (inter-monomer) was also analysed. The interaction energy between the N-finger and domain III of different monomers as a function of time is presented in Fig. S22. As in the previous section, additional detailed information regarding inter-monomer interactions is also available in Supplementary Material, together with visual representations of the observed interactome for all analysed M^{pro} variants (Figs. S23–S31, Table S7).

Overall, most mutants have decreased interaction energies. The exception is mutant R298Q (representation of structural arrangement is presented in Fig. 5) and at 2 points in time, also R298A.

It is not unexpected that these mutants show interaction energies on the same magnitude as WT M^{pro}. However, R298Q can achieve

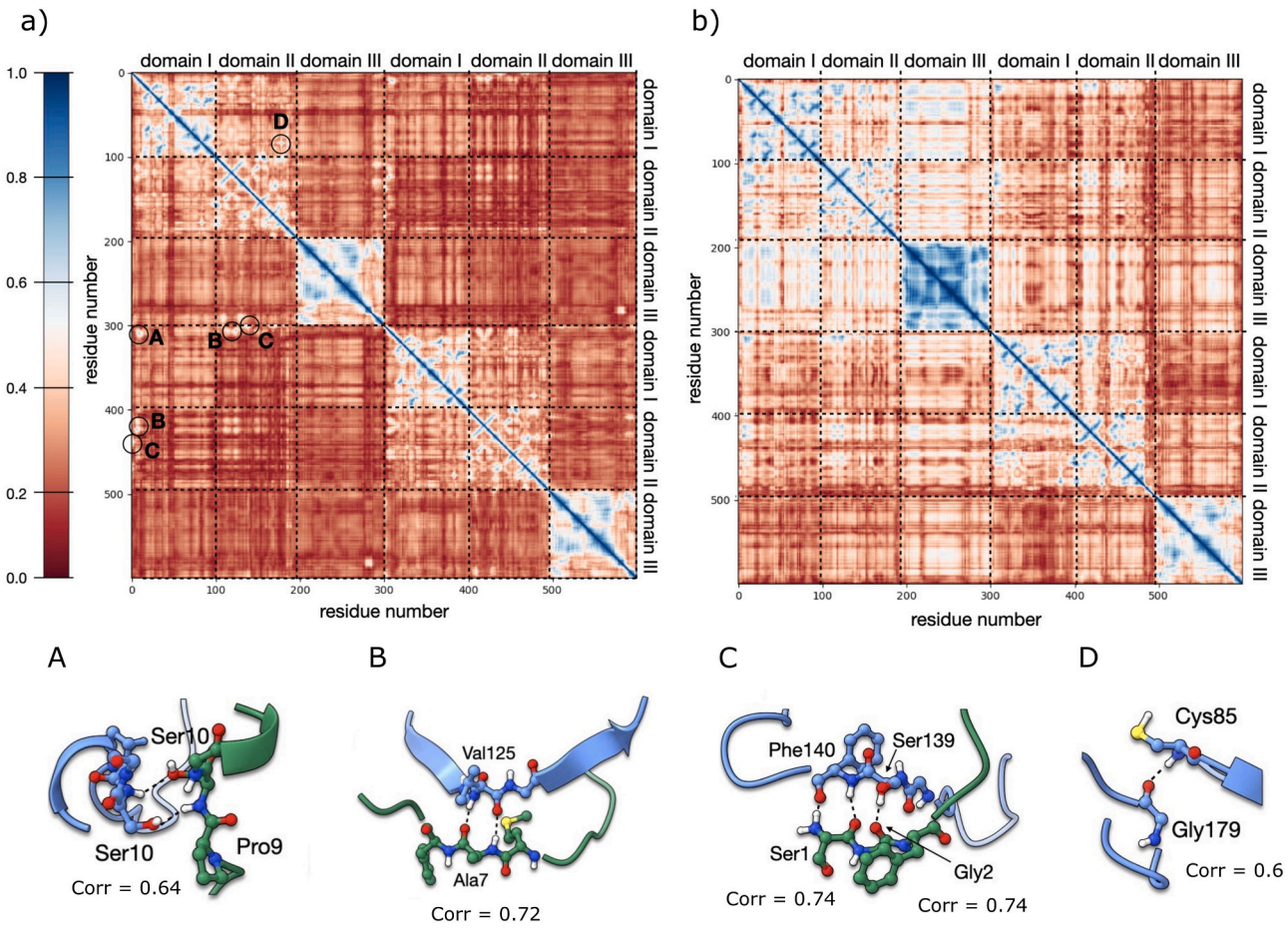

Fig. 4. The gCorrelation plot for a) WT M^{pro} and b) R4Q R298Q SARS-CoV-2 M^{pro} with the representation of the most prominent inter-residue correlations (A-D) for WT M^{pro} (below gCorrelation plots, different protein chain colors represent different monomers). The gCorrelation plot for the double glutamine mutant presents an increased inter-residue correlation. The gCorrelation map of WT M^{pro} dimer shows well-conserved blocks of correlation (color blue). The darkest blue color represents the maximal possible correlation with itself and is observed in the main diagonal of the matrix. The upper-left quadrant (residue numbers 0–300) corresponds to one M^{pro} molecule in the dimer - for simplicity, the monomer, though here we refer to the monomer in the dimer - whereas the lower-right quadrant (residues 300–600) corresponds to the other monomer. The other two quadrants describe the interaction between monomers. For reference, the average correlation value for M^{pro} WT is 0.27, whereas for the double glutamine mutant the average correlation is 0.40.

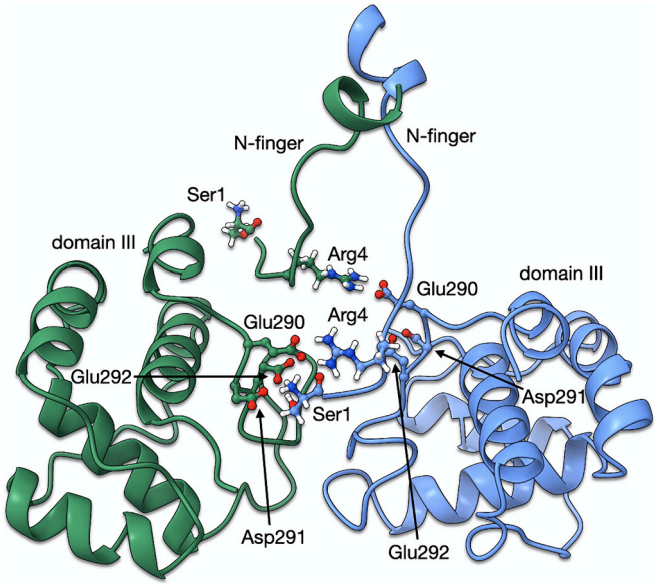

Fig. 5. Representation of the global minimum of interaction energy recorded for the R298Q mutant at 350 ns of simulation time.

interaction energies almost 10 kcal/mol lower than the WT protein. Further, on the other half of the dimer, not only does this mutant reach interaction energies lower by a factor of 3, but also double mutants seem to show increased dynamic stability. This prompted a search for the root of such additional stabilization, which was easily traced to interactions between the N-terminus of Ser1 and Arg4 (if present) with Glu290, Asp291, and Glu292. For the double mutants, the respective stability is achieved *via* Ser1's ammonium group exclusively, showing that the participation of Arg4 is not always required for observing the over-stabilized interactions. When not interacting with the carboxylate groups mentioned before, Ser1 establishes ionic bridges and hydrogen bonds with Glu166, which is diametrically opposite to domain III (Fig. S22a)). Though the quantum mechanical calculations included only a significantly reduced portion of M^{pro} and its dimer, they indicate that even if the interaction energy between different monomers is not impacted, the mutations studied significantly affect the internal stability of the monomers, therefore negatively impacting the entropy of binding associated with the dimerization process.

Considering the data collectively, this indicates that, by increasing the entropic content of the monomeric state of M^{pro}, the entropic content of the dimer might also increase, otherwise binding might be prevented. By increasing the entropic content of the dimer, the stability of the active site is sacrificed, reducing the catalytic activity.

4. Discussion

We comprehensively analysed the structural and functional aspects of the SARS-CoV-2 M^{pro} dimerization process. M^{pro} is unequivocally one of the vital elements of the viral replication machinery, which cannot be circumvented by alternative pathways, as evidenced by the clinical success of nirmatrelvir [45,46]. Although this therapeutic strategy is readily applicable and has demonstrated its value, the widespread use of protease inhibitors leads to the emergence of drug resistance, affecting other drugs with a similar mode of action.

Our study on the mechanism of M^{pro} dimerization deepens our understanding on how dimerization may disrupt the enzyme's activity. The literature has already demonstrated the existence of key interface residues, modifications of which can lead to the severe disruption of M^{pro} proteolytic activity, and consequently the inhibition of SARS-CoV's replication.

The N-finger region (Ser1-Ala7) is essential for catalytic activity and dimerization of M^{pro}. The N-terminus of one monomer is inserted between domains II and III of the second subunit [2,10,47–49], where it interacts with Glu166 and it enables the proper arrangement of the S1 substrate binding pocket. Several studies indicate that deletion of the 1–7 region in SARS-CoV M^{pro} hampers dimerization [50], however others showed, that M^{pro} deprived of the N-finger is functional and dimerizes through domain III. This, however, results in significant loss of its activity [49]. Further, it was shown that the removal of the first three residues from the N-terminus of SARS-CoV M^{pro} allows for the dimer formation, with only 24 % loss of activity. When the next four residues were removed (Arg4-Ala7), both the activity and dimerization were significantly hindered. It is known that Arg4 forms hydrogen bonds and a salt bridge with Glu290, and this interaction is pointed out as essential regarding dimer formation and stabilization. Thus, it has been postulated that blocking this interaction could significantly affect M^{pro} activity and disrupt the dimer interface - however, the role of Arg4 for the M^{pro} dimerization and/or regulation of the activity remains questionable. It was demonstrated that mutation of Arg4 to Ala or Glu resulted in inhibition of the proteolytic activity of SARS-CoV-2 M^{pro}, yet the enzyme was still present in a dimeric form [51]. On the other hand, it was previously shown that the mutation of Arg4 in SARS-CoV M^{pro} does not affect the enzyme's activity itself, but its effectiveness in dimerizing, which was observed as a 4.5-fold increase in K_D values [52]. Further, recent findings indicate that N-terminal processing is important for correct protein folding, though it is not essential for dimerization [53].

In the present study, considering the above-mentioned discrepancies, an attempt was made to evaluate the effect of Arg4 on dimer formation and thus on the regulation of SARS-CoV-2 M^{pro} activity. According to the data, it can be observed that although some differences between WT M^{pro} and Arg4-modified variants exist, all these forms are capable of dimerizing at nanomolar concentrations, in agreement with the substrate processing data. However, as a significant decrease in the effective activity was observed for R4A and R4Q M^{pro}, with similar MSA values observed at the same time, a much greater contribution of dimerization process as a component affecting the formation of a functional enzyme is indicated. The aforementioned dependence is also present in the case of other analysed mutants, where with the observed reduction in MSA, a substantial drop in EA is evident, differing by up to three orders of magnitude compared with EA values determined for WT M^{pro}. Considering also the fact, that proper dimer formation is essential for the correct arrangement of the substrate-binding cleft [2,54], it can be concluded that interference with dimer formation is the primary factor driving the reduction in substrate processing efficiency.

M^{pro} R4A and R4Q mutations result particularly in the disruption of the interactions between two distinct monomers in the M^{pro} dimers - mutation of Arg4 suppresses a prominent hydrogen bond and ionic bridge with Glu290. The replacement of Arg by Gln silences the salt bridge component of the interaction. It also weakens the hydrogen bond interaction, because of increased partial charges in the amide's nitrogen. This is the main root of the synergistic effect between hydrogen bonds and charge in the interaction for WT M^{pro}. The replacement of Arg by Ala completely silences both interactions. The experimental data show that, though impairing the apparent dimerization equilibrium constant, the effect of this single mutation on the dimer stability is not as prominent, as that of mutations in Arg298. The molecular dynamics simulations revealed that the R4A and R4Q mutations indeed affect the overall interaction energy between the N-finger and the C-domain. Still, in one particular subset of interactions in the dimer, the ability of the R4A mutant to reach lower interaction energies between the two domains specified above was observed. This is due to additional interaction pockets occurring during the molecular dynamic simulations. Interestingly, these interaction pockets were not observed for the R4Q mutant, where a remnant of the native interaction with Glu290 is still present. This leads to the conclusion that completely disturbing the formation of the residue 4 - Glu290 salt bridge allows the system to easily access novel interaction pockets, where the N-terminus of Ser1 interacts with the carboxylate triangle formed by Glu290, Asp291, and Glu292. This seems to be a prominent interaction that is possible for all M^{pro} variants here studied, which would then justify, why mutations on Arg4 do not exhibit a stronger impact on the dimerization constants and MSA values. Based on the simulation, it is shown that shortening or even extending the N-terminus of M^{pro} should have a significant impact on the ability of the protein to dimerize. Taken together, our study indicates Arg4 as a minor player in SARS-COV-2 M^{pro} dimer formation, as evident from K_D constants, mass photometry measurements, and MD data.

As previously discussed, M^{pro}'s C-domain, more specifically the residues Glu290-Gln299, is another region of interest in the context of M^{pro}'s ability to oligomerize [13,55]. Multiple efforts have been directed towards understanding the domain III and its function [2,8,12,13,15,16,24,48,49,51,52,56]. The C-domain, together with the N-terminus, regulates the dimerization of M^{pro}; notably, it also possesses the capability for self-dimerization. It should be noted, however, that the dimer formed only by domain III alone differs from the typical active dimer organization of M^{pro}, suggesting the formation of the altered dimeric form [49]. Several residues of domain III have been indicated as critical for SARS-CoV M^{pro} dimerization. This includes Glu290, which forms an ionic interaction with Arg4, discussed above. Variant E290A caused significant loss of activity and impaired dimerization (K_D values even 28,5-fold higher when compared to the WT enzyme) [52]. It is worth mentioning that besides the Arg4-Glu290 pair, a modification of Glu290 was proved to play a major role in disrupting the enzyme's activity, consistent with the limited role of Arg4 described above. The role of Glu290 for dimerization was also previously demonstrated, where Glu290 substitution to Ala led to significantly higher dimer dissociation constants [16]. Further, it was established that out of 15 variants, including Glu288A, Asp289A, Glu290A, Arg298A, and Gln299A, all were detrimental to the enzymatic activity of M^{pro} [15].

Based on the literature, Arg298 is thought to be one of the essential elements affecting dimer formation and enzyme activity. According to the previous reports, Arg298 serves both as inter- and intra-monomer binding partner. The inter-monomer interaction between Arg298 and Ser123 stabilizes the dimer. The intra-monomer interaction of Arg298 with Met6 further affects the correct orientation of Tyr126 and Phe140 of the opposite monomer and leads to the correct formation of the substrate binding pocket. The most affected region is the S1 sub-site, which is critical for enzymatic activity. This highlights the importance of the interaction Arg298-Met6 [6,16,50,57–59]. Besides, according to the literature data, Arg298 was also found to be located in the attractive, druggable pocket. Two fragments binding near Arg298 (third fragment targeting region proximal to Arg4) and the decrease of enzymatic activity upon fragment binding at that location were described [7]. Among several druggable pockets in the M^{pro} structure identified by L. Alzyoud et al., Arg298 region was the second-best spot identified in this study [60]. Further, a dimerization-interfering drug candidate x1187 was found to bind within the pocket near Arg298 and N-finger region and

effectively blocked M^{pro} dimerization under 10-fold molar excess [61]. These data additionally indicate the importance of Arg298 region as an attractive and feasible target for therapy.Mutations involving R298 are known to result in monomeric M^{pro} forms, with noticeable loss, or even complete abolishment of enzymatic activity [2,6,47,48,52,57,62,63]. In the monomeric crystal structure of the SARS-CoV R298A M^{pro} variant, residues Ser139-Leu141 form a 3_{10}-helix, instead of the loop, which is characteristic of dimeric forms [57]. This helical structure subsequently triggers the movement of the N142 side chain, leading to its interaction with E166 and obstructing access to the S1 subsite [16,47]. Interestingly, it was reported, that monomeric SARS-CoV R298 mutant can dimerize *via* substrate-induced dimerization, resulting in a functional form with enzymatic activity comparable to WT enzymes [11].

Our experimental data indeed demonstrate, that there is both a disruption of dimer formation and the aberrant arrangement of the active site and/or substrate-binding pocket of M^{pro} R298A and R298Q mutants, resulting in a significant loss of activity. However, these two mutations do not directly impact the inter-monomer interactions in the dimer, since Arg298 interacts primarily with residues from the same chain. Nonetheless, these mutants exhibit lower dimer stability in comparison to the mutations directly impacting the interaction surface of different monomers. Calculations performed on the intra-monomer interactions between N-finger and domain III show that all mutants exhibit lower interaction energies, when compared to WT M^{pro}. This points to an imbalance in the enthalpy and entropy contributions to dimerization resulting from the internal energetics of the monomers. Further, though these results should be analysed cautiously since the analysis was restricted to results of two specific domains, it is observed that mutations of Arg298 have an overall more prominent impact on the intra-monomer N-finger-C-domain interactions, than mutations of Arg4. The influence of the extended N-finger is also quite prominent from the data collected using dynamical traces. This underscores the primary consequence derived from the calculations – mutations explored in this work affect primarily the intra-monomer interactions between C-domain and the N-finger. This might at first seem counterintuitive, as the focus is on the ability of M^{pro} to form dimers. However, when bringing the MD simulations and the quantum mechanical evaluation of those traces together, a fine balance between the internal stability of the M^{pro} monomer, and the ease of the dimerization emerges. It is, therefore, concluded that while the studied mutations have no impact on the absolute enthalpies of dimerization, they do have a preponderant effect on entropies of binding. Consequently, the dimer stability is impaired, and hence – also the catalytic power of the active site.

Taking the above information together, one concludes that in the case of SARS-CoV-2 M^{pro}, the residue R298 undoubtedly plays an important role in maintaining the dimerized state. As evidenced by experimental data and supported by the computational studies, it is shown clearly that Arg298 is critical for intra-monomer rigidity, significantly affecting the stability of the monomer. This further affects dimerization and inter-monomer interactions.

Although the mutation of Arg4 alone is not associated with a strong hindrance of dimerization, the double mutation of Arg4 and Arg298 indeed exhibits synergistically devastating consequences: the oligomerization ability and enzymatic activity of the protease are completely abolished. Our SARS-CoV-2 M^{pro} double mutant experiments clearly showed the strong impact that the direct and indirect effects of mutations on Arg298 and Arg4 have on the monomer stability. From the computational perspective, these are also mutants exhibiting more pronounced structural variations, translated to loss of rigidity. The impact of mutations on the active site is clear from the simulations. The thermodynamic mechanism of the impact of mutations on the fine balance between enthalpy and entropy emerges from the combined molecular and quantum mechanical evaluations. Regardless of the mutant analysed, the internal interactions between N-finger and domain III are affected.

From the fact that mutation of an Arg has such a strong impact on overall stability, a residue with a flexible side chain, it is hypothesized that this and other residues that are bridging different M^{pro} domains are acting like a suspension system, controlling the holding and handling between the different M^{pro} domains. This suspension is critical for keeping the internal motions of each domain contained within themselves, avoiding transmitting such vibrations to other parts of the molecule. Silencing or weakening this suspension naturally leads to stronger interference between the different domains, culminating in the arhythmic-like behavior observed in the analysis of the gCorrelation. This interpretation brings about a fascinating link between the mechanics of purely man-made systems and those of biological nature, showing the evolutionary refinement that led to one of the most efficient types of machinery observed in viruses.

The importance of understanding the dimerization of the main protease (M^{pro}) of SARS-CoV-2 cannot be underestimated in the context of developing effective antiviral therapeutic strategies. Presented research systematically illustrates the significance of M^{pro} dimerization for its enzymatic activity, thereby highlighting the dimerization interface as a potential target for novel antiviral interventions. Previous studies, including crystallographic fragment screening approaches, have proposed small fragments capable of binding within hydrophobic pockets formed by specific amino acid sidechains within the M^{pro} structure, notably Met6, Phe8, Arg298, and Val303, or Gly2, Arg4, Phe3, and Lys5 patches [7]. Others have been identified using, for example, mass spectrometry-based assays to be capable of disrupting M^{pro} dimerization, but no specific amino acids involved in binding were shown [61]. However, despite these advancements, none of the proposed fragments have been developed into fully effective “hit” compounds. Thus, comprehensive systematic work, such as the one presented by us integrating mutational and enzymatic studies, is imperative to identify critical “hot points” within the M^{pro} structure, facilitating the design of targeted therapeutic interventions against SARS-CoV-2.

5. Conclusions

According to our study, Arg4 in SARS-CoV-2 M^{pro} is not the main driver for dimerization and high enzyme activity, proving that disruption of only the Arg4-Glu290 salt bridge is insufficient to inhibit organization of the SARS-CoV-2 M^{pro} dimer. However, mutation of SARS-CoV-2 M^{pro} Arg298, which involves the disruption of the Arg 298-Ser123/Met6 interaction, completely abolishes the dimer formation and results in significant activity loss. The simultaneous modification of these two residues, affecting two critical regions and covering both inter- and intra-monomer interactions, resulted in detrimental effects. Even more strikingly, this effect is observed at both, high enzyme and saturating substrate concentrations, indicating that potentially substrate-induced dimerization is affected as well.

The presented research organizes and deepens our knowledge of the potential of inhibition of M^{pro}'s enzymatic activity by preventing dimerization, offering complementary approaches to limit SARS-CoV-2 virulence. This provides a new perspective, suggesting that targeted therapies can hit the weakest point, or rather - the most critical parts of the enzyme machinery. Moreover, given the high conservation of M^{pro}, the findings presented may prove to be universal and can serve as a versatile approach to control the spread and pathogenic potential of novel coronaviruses.

CRediT authorship contribution statement

Kinga Lis: Writing – review & editing, Writing – original draft, Visualization, Validation, Methodology, Investigation, Formal analysis. **Jacek Plewka:** Writing – review & editing, Visualization, Validation, Methodology. **Filipe Menezes:** Writing – review & editing, Visualization, Methodology, Investigation. **Ewa Bielecka:** Validation, Methodology, Investigation. **Yuliya Chykunova:** Writing – review & editing, Methodology, Investigation. **Katarzyna Pustelny:** Writing – review &

editing, Methodology, Investigation. **Stephan Niebling:** Writing – review & editing, Methodology, Investigation. **Angelica Struve Garcia:** Writing – review & editing, Methodology, Investigation. **Maria Garcia-Alai:** Writing – review & editing, Methodology, Investigation. **Grzegorz M. Popowicz:** Writing – review & editing, Validation, Methodology. **Anna Czarna:** Writing – review & editing, Funding acquisition, Formal analysis, Conceptualization. **Tomasz Kantyka:** Writing – review & editing, Supervision, Funding acquisition, Formal analysis, Conceptualization. **Krzysztof Pyrc:** Writing – review & editing, Supervision, Project administration, Funding acquisition, Formal analysis, Conceptualization.

Declaration of competing interest

The authors declare that they have no known competing financial interests or personal relationships that could have appeared to influence the work reported in this paper.

Acknowledgments

This work was supported by a subsidy from the Polish Ministry of Science and Higher Education for research on SARS-CoV-2, a grant from the National Science Center (UMO-2017/27/B/NZ6/02488), the Corona Accelerated R&D in Europe (CARE) project funded by the Innovative Medicines Initiative two Joint Undertaking (JU) under grant agreement no. 101005077, the DURABLE project, co-funded by the European Union, under the EU4Health Programme (EU4H) (https://health.ec.europa.eu/funding/eu4health-programme-2021-2027-vision-health iereuropean-union_en#work-programmes) (all to K.P.), by Norway Financial Mechanism for years 2014 - 2021 under the GRIEG Project (2019/34/H/NZ1/00674 to T.K.), and by grant from the National Science Centre (UMO-2019/34/E/NZ1/00467) and NAWA Polish Returns 2018 (PPN/PPO/2018/1/00046/U/00001) to AC; We acknowledge the MCB Structural Biology Core Facility (supported by the TEAM TECH CORE FACILITY/ 2017-4/6 grant from the Foundation for Polish Science) for valuable support. We acknowledge the European Synchrotron Radiation Facility (ESRF) for provision of synchrotron radiation facilities. We acknowledge DESY (Hamburg, Germany), a member of the Helmholtz Association HGF, for the provision of experimental facilities. We thank the Helmholtz-Zentrum Berlin für Materialien und Energie for the allocation of synchrotron radiation beam time. The study was carried out using research infrastructure funded by the European Union in the framework of the Smart Growth Operational Programme, Measure 4.2; Grant No. POIR.04.02.00-00-D001/20, "ATOMIN 2.0 – Center for materials research on ATOMic scale for the INnovative economy.

Appendix A. Supplementary data

Supplementary data to this article can be found online at https://doi.org/10.1016/j.ijbiomac.2024.131392.

References

[1] WHO Coronavirus (COVID-19), Dashboard, 2023.
[2] B. Goyal, D. Goyal, Targeting the dimerization of the Main protease of coronaviruses: a potential broad-Spectrum therapeutic strategy, ACS Comb. Sci. 22 (2020) 297–305, https://doi.org/10.1021/acscombsci.0c00058.
[3] Q. Hu, Y. Xiong, G. Zhu, Y. Zhang, Y. Zhang, P. Huang, G. Ge, The SARS-CoV-2 main protease (M ^{pro}): structure, function, and emerging therapies for COVID-19, MedComm (Beijing) 3 (2022), https://doi.org/10.1002/mco2.151.
[4] Z. Jin, X. Du, Y. Xu, Y. Deng, M. Liu, Y. Zhao, B. Zhang, X. Li, L. Zhang, C. Peng, Y. Duan, J. Yu, L. Wang, K. Yang, F. Liu, R. Jiang, X. Yang, T. You, X. Liu, X. Yang, F. Bai, H. Liu, X. Liu, L.W. Guddat, W. Xu, G. Xiao, C. Qin, Z. Shi, H. Jiang, Z. Rao, H. Yang, Structure of Mpro from SARS-CoV-2 and discovery of its inhibitors, Nature 582 (2020) 289–293, https://doi.org/10.1038/s41586-020-2223-y.
[5] Q. Hu, Y. Xiong, G. Zhu, Y. Zhang, Y. Zhang, P. Huang, G. Ge, The SARS-CoV-2 main protease (M ^{pro}): structure, function, and emerging therapies for COVID-19, MedComm (Beijing) 3 (2022), https://doi.org/10.1002/mco2.151.
[6] T. Hu, Y. Zhang, L. Li, K. Wang, S. Chen, J. Chen, J. Ding, H. Jiang, X. Shen, Two adjacent mutations on the dimer interface of SARS coronavirus 3C-like protease cause different conformational changes in crystal structure, Virology 388 (2009) 324–334, https://doi.org/10.1016/j.virol.2009.03.034.
[7] A. Douangamath, D. Fearon, P. Gehrtz, T. Krojer, P. Lukacik, C.D. Owen, E. Resnick, C. Strain-Damerell, A. Aimon, P. Ábrányi-Balogh, J. Brandão-Neto, A. Carbery, G. Davison, A. Dias, T.D. Downes, L. Dunnett, M. Fairhead, J.D. Firth, S. P. Jones, A. Keeley, G.M. Keserü, H.F. Klein, M.P. Martin, M.E.M. Noble, P. O'Brien, A. Powell, R.N. Reddi, R. Skyner, M. Snee, M.J. Waring, C. Wild, N. London, F. von Delft, M.A. Walsh, Crystallographic and electrophilic fragment screening of the SARS-CoV-2 main protease, Nat. Commun. 11 (2020) 5047, https://doi.org/10.1038/s41467-020-18709-w.
[8] G.D. Noske, A.M. Nakamura, V.O. Gawriljuk, R.S. Fernandes, G.M.A. Lima, H.V. D. Rosa, H.D. Pereira, A.C.M. Zeri, A.F.Z. Nascimento, M.C.L.C. Freire, D. Fearon, A. Douangamath, F. von Delft, G. Oliva, A.S. Godoy, A crystallographic snapshot of SARS-CoV-2 Main protease maturation process, J. Mol. Biol. 433 (2021) 167118, https://doi.org/10.1016/j.jmb.2021.167118.
[9] S.E. Greasley, S. Noell, O. Plotnikova, R. Ferre, W. Liu, B. Bolanos, K. Fennell, J. Nicki, T. Craig, Y. Zhu, A.E. Stewart, C.M. Steppan, Structural basis for the in vitro efficacy of nirmatrelvir against SARS-CoV-2 variants, J. Biol. Chem. 298 (2022) 101972, https://doi.org/10.1016/j.jbc.2022.101972.
[10] J. Lee, C. Kenward, L.J. Worrall, M. Vuckovic, F. Gentile, A.-T. Ton, M. Ng, A. Cherkasov, N.C.J. Strynadka, M. Paetzel, X-ray crystallographic characterization of the SARS-CoV-2 main protease polyprotein cleavage sites essential for viral processing and maturation, Nat. Commun. 13 (2022) 5196, https://doi.org/10.1038/s41467-022-32854-4.
[11] C.-G. Wu, S.-C. Cheng, S.-C. Chen, J.-Y. Li, Y.-H. Fang, Y.-H. Chen, C.-Y. Chou, Mechanism for controlling the monomer–dimer conversion of SARS coronavirus main protease, Acta Crystallogr. D Biol. Crystallogr. 69 (2013) 747–755, https://doi.org/10.1107/S0907444913001315.
[12] K. Anand, Structure of coronavirus main proteinase reveals combination of a chymotrypsin fold with an extra alpha-helical domain, EMBO J. 21 (2002) 3213–3224, https://doi.org/10.1093/emboj/cdf327.
[13] J. Shi, Z. Wei, J. Song, Dissection study on the severe acute respiratory syndrome 3C-like protease reveals the critical role of the extra domain in dimerization of the enzyme, J. Biol. Chem. 279 (2004) 24765–24773, https://doi.org/10.1074/jbc.M311744200.
[14] N.T. Nashed, D.W. Kneller, L. Coates, R. Ghirlando, A. Aniana, A. Kovalevsky, J. M. Louis, Autoprocessing and oxyanion loop reorganization upon GC373 and nirmatrelvir binding of monomeric SARS-CoV-2 main protease catalytic domain, Commun Biol 5 (2022) 976, https://doi.org/10.1038/s42003-022-03910-y.
[15] J. Shi, J. Song, The catalysis of the SARS 3C-like protease is under extensive regulation by its extra domain, FEBS J. 273 (2006) 1035–1045, https://doi.org/10.1111/j.1742-4658.2006.05130.x.
[16] N.T. Nashed, A. Aniana, R. Ghirlando, S.C. Chiliveri, J.M. Louis, Modulation of the monomer-dimer equilibrium and catalytic activity of SARS-CoV-2 main protease by a transition-state analog inhibitor, Commun Biol 5 (2022) 160, https://doi.org/10.1038/s42003-022-03084-7.
[17] A. Citarella, A. Scala, A. Piperno, N. Micale, SARS-CoV-2 Mpro: a potential target for Peptidomimetics and small-molecule inhibitors, Biomolecules 11 (2021) 607, https://doi.org/10.3390/biom11040607.
[18] A. Citarella, A. Dimasi, D. Moi, D. Passarella, A. Scala, A. Piperno, N. Micale, Recent advances in SARS-CoV-2 Main protease inhibitors: from Nirmatrelvir to future perspectives, Biomolecules 13 (2023) 1339, https://doi.org/10.3390/biom13091339.
[19] D.R. Owen, C.M.N. Allerton, A.S. Anderson, L. Aschenbrenner, M. Avery, S. Berritt, B. Boras, R.D. Cardin, A. Carlo, K.J. Coffman, A. Dantonio, L. Di, H. Eng, R. Ferre, K.S. Gajiwala, S.A. Gibson, S.E. Greasley, B.L. Hurst, E.P. Kadar, A.S. Kalgutkar, J. C. Lee, J. Lee, W. Liu, S.W. Mason, S. Noell, J.J. Novak, R.S. Obach, K. Ogilvie, N. C. Patel, M. Pettersson, D.K. Rai, M.R. Reese, M.F. Sammons, J.G. Sathish, R.S. P. Singh, C.M. Steppan, A.E. Stewart, J.B. Tuttle, L. Updyke, P.R. Verhoest, L. Wei, Q. Yang, Y. Zhu, An oral SARS-CoV-2 M ^{pro} inhibitor clinical candidate for the treatment of COVID-19, Science 374 (2021) (1979) 1586–1593, https://doi.org/10.1126/science.abl4784.
[20] Y. Hu, E.M. Lewandowski, H. Tan, X. Zhang, R.T. Morgan, X. Zhang, L.M.C. Jacobs, S.G. Butler, M.V. Gongora, J. Choy, X. Deng, Y. Chen, J. Wang, Naturally occurring mutations of SARS-CoV-2 Main protease confer drug resistance to Nirmatrelvir, ACS Cent. Sci. 9 (2023) 1658–1669, https://doi.org/10.1021/acscentsci.3c00538.
[21] S.A. Moghadasi, E. Heilmann, A.M. Khalil, C. Nnabuife, F.L. Kearns, C. Ye, S. N. Moraes, F. Costacurta, M.A. Esler, H. Aihara, D. von Laer, L. Martinez-Sobrido, T. Palzkill, R.E. Amaro, R.S. Harris, Transmissible SARS-CoV-2 variants with resistance to clinical protease inhibitors, Sci. Adv. 9 (2023), https://doi.org/10.1126/sciadv.ade8778.
[22] R.P. Joyce, V.W. Hu, J. Wang, The history, mechanism, and perspectives of nirmatrelvir (PF-07321332): an orally bioavailable main protease inhibitor used in combination with ritonavir to reduce COVID-19-related hospitalizations, Med. Chem. Res. 31 (2022) 1637–1646, https://doi.org/10.1007/s00044-022-02951-6.
[23] J.T. Lee, Q. Yang, A. Gribenko, B.S. Perrin, Y. Zhu, R. Cardin, P.A. Liberator, A. S. Anderson, L. Hao, Genetic surveillance of SARS-CoV-2 M ^{pro} reveals high sequence and structural conservation prior to the introduction of protease inhibitor Paxlovid, MBio 13 (2022), https://doi.org/10.1128/mbio.00869-22.
[24] S. Kaptan, M. Girych, G. Enkavi, W. Kulig, V. Sharma, J. Vuorio, T. Rog, I. Vattulainen, Maturation of the SARS-CoV-2 virus is regulated by dimerization of its main protease, Comput Struct, Biotechnol. J. 20 (2022) 3336–3346, https://doi.org/10.1016/j.csbj.2022.06.023.
[25] J.D. Ip, A. Wing-Ho Chu, W.-M. Chan, R. Cheuk-Ying Leung, S.M. Umer Abdullah, Y. Sun, K.K.-W., To, global prevalence of SARS-CoV-2 3CL protease mutations

associated with nirmatrelvir or ensitrelvir resistance, EBioMedicine 91 (2023) 104559, https://doi.org/10.1016/j.ebiom.2023.104559.
[26] M.D. Sacco, Y. Hu, M.V. Gongora, F. Meilleur, M.T. Kemp, X. Zhang, J. Wang, Y. Chen, The P132H mutation in the main protease of omicron SARS-CoV-2 decreases thermal stability without compromising catalysis or small-molecule drug inhibition, Cell Res. 32 (2022) 498–500, https://doi.org/10.1038/s41422-022-00640-y.
[27] S. Niebling, K. Veith, B. Vollmer, J. Lizarrondo, O. Burastero, J. Schiller, A. Struve García, P. Lewe, C. Seuring, S. Witt, M. García-Alai, Biophysical screening pipeline for Cryo-EM grid preparation of membrane proteins, Front. Mol. Biosci. 9 (2022), https://doi.org/10.3389/fmolb.2022.882288.
[28] O. Burastero, S. Niebling, L.A. Defelipe, C. Günther, A. Struve, M.M., Garcia Alai, eSPC: an online data-analysis platform for molecular biophysics, Acta Crystallogr D Struct Biol 77 (2021) 1241–1250, https://doi.org/10.1107/S2059798321008998.
[29] W. Kabsch, XDS, Acta Crystallogr. D Biol. Crystallogr. 66 (2010) 125–132, https://doi.org/10.1107/S0907444909047337.
[30] A.J. McCoy, R.W. Grosse-Kunstleve, P.D. Adams, M.D. Winn, L.C. Storoni, R. J. Read, Phaser crystallographic software, J. Appl. Cryst. 40 (2007) 658–674, https://doi.org/10.1107/S0021889807021206.
[31] P. Emsley, B. Lohkamp, W.G. Scott, K. Cowtan, Features and development of coot, Acta Crystallogr. D Biol. Crystallogr. 66 (2010) 486–501, https://doi.org/10.1107/S0907444910007493.
[32] R.P. Joosten, F. Long, G.N. Murshudov, A. Perrakis, The PDB_REDO server for macromolecular structure model optimization, IUCrJ 1 (2014) 213–220, https://doi.org/10.1107/S2052252514009324.
[33] E.F. Pettersen, T.D. Goddard, C.C. Huang, G.S. Couch, D.M. Greenblatt, E.C. Meng, T.E. Ferrin, UCSF chimera—a visualization system for exploratory research and analysis, J. Comput. Chem. 25 (2004) 1605–1612, https://doi.org/10.1002/jcc.20084.
[34] M.J. Abraham, T. Murtola, R. Schulz, S. Páll, J.C. Smith, B. Hess, E. Lindahl, GROMACS: high performance molecular simulations through multi-level parallelism from laptops to supercomputers, SoftwareX 1–2 (2015) 19–25, https://doi.org/10.1016/j.softx.2015.06.001.
[35] J. Huang, A.D. MacKerell, CHARMM36 all-atom additive protein force field: validation based on comparison to NMR data, J. Comput. Chem. 34 (2013) 2135–2145, https://doi.org/10.1002/jcc.23354.
[36] A.D. MacKerell, D. Bashford, M. Bellott, R.L. Dunbrack, J.D. Evanseck, M.J. Field, S. Fischer, J. Gao, H. Guo, S. Ha, D. Joseph-McCarthy, L. Kuchnir, K. Kuczera, F.T. K. Lau, C. Mattos, S. Michnick, T. Ngo, D.T. Nguyen, B. Prodhom, W.E. Reiher, B. Roux, M. Schlenkrich, J.C. Smith, R. Stote, J. Straub, M. Watanabe, J. Wiórkiewicz-Kuczera, D. Yin, M. Karplus, All-atom empirical potential for molecular modeling and dynamics studies of proteins, J. Phys. Chem. B 102 (1998) 3586–3616, https://doi.org/10.1021/jp973084f.
[37] J. Lemkul, From proteins to perturbed Hamiltonians: a suite of tutorials for the GROMACS-2018 molecular simulation package [article v1.0], Living J Comput Mol Sci 1 (2019), https://doi.org/10.33011/livecoms.1.1.5068.
[38] O.F. Lange, H. Grubmüller, Generalized correlation for biomolecular dynamics, proteins: structure, Function, and Bioinformatics 62 (2006) 1053–1061, https://doi.org/10.1002/prot.20784.
[39] F. Menezes, G.M. Popowicz, *ULYSSES* : an efficient and easy to use Semiempirical library for C++, J. Chem. Inf. Model. 62 (2022) 3685–3694, https://doi.org/10.1021/acs.jcim.2c00757.
[40] C. Bannwarth, S. Ehlert, S. Grimme, GFN2-xTB—an accurate and broadly parametrized self-consistent tight-binding quantum chemical method with multipole electrostatics and density-dependent dispersion contributions, J. Chem. Theory Comput. 15 (2019) 1652–1671, https://doi.org/10.1021/acs.jctc.8b01176.
[41] S. Ehlert, M. Stahn, S. Spicher, S. Grimme, Robust and efficient implicit solvation model for fast Semiempirical methods, J Chem Theory Comput 17 (2021) 4250–4261, https://doi.org/10.1021/acs.jctc.1c00471.
[42] E.F. Pettersen, T.D. Goddard, C.C. Huang, E.C. Meng, G.S. Couch, T.I. Croll, J. H. Morris, T.E. Ferrin, <scp>UCSF ChimeraX</scp> : structure visualization for researchers, educators, and developers, Protein Sci. 30 (2021) 70–82, https://doi.org/10.1002/pro.3943.
[43] T.D. Goddard, C.C. Huang, E.C. Meng, E.F. Pettersen, G.S. Couch, J.H. Morris, T. E. Ferrin, U.C.S.F. ChimeraX, Meeting modern challenges in visualization and analysis, Protein Sci. 27 (2018) 14–25, https://doi.org/10.1002/pro.3235.
[44] D. Wu, G. Piszczek, Standard protocol for mass photometry experiments, Eur. Biophys. J. 50 (2021) 403–409, https://doi.org/10.1007/s00249-021-01513-9.
[45] C. Huang, H. Shuai, J. Qiao, Y. Hou, R. Zeng, A. Xia, L. Xie, Z. Fang, Y. Li, C. Yoon, Q. Huang, B. Hu, J. You, B. Quan, X. Zhao, N. Guo, S. Zhang, R. Ma, J. Zhang, Y. Wang, R. Yang, S. Zhang, J. Nan, H. Xu, F. Wang, J. Lei, H. Chu, S. Yang, A new generation Mpro inhibitor with potent activity against SARS-CoV-2 omicron variants, Signal Transduct. Target. Ther. 8 (2023) 128, https://doi.org/10.1038/s41392-023-01392-w.
[46] B.-X. Quan, H. Shuai, A.-J. Xia, Y. Hou, R. Zeng, X.-L. Liu, G.-F. Lin, J.-X. Qiao, W.-P. Li, F.-L. Wang, K. Wang, R.-J. Zhou, T.T.-T. Yuen, M.-X. Chen, C. Yoon, M. Wu, S.-Y. Zhang, C. Huang, Y.-F. Wang, W. Yang, C. Tian, W.-M. Li, Y.-Q. Wei, K.-Y. Yuen, J.F.-W. Chan, J. Lei, H. Chu, S. Yang, An orally available Mpro inhibitor is effective against wild-type SARS-CoV-2 and variants including omicron, Nat. Microbiol. 7 (2022) 716–725, https://doi.org/10.1038/s41564-022-01119-7.
[47] D. Suárez, N. Díaz, SARS-CoV-2 Main protease: a molecular dynamics study, J. Chem. Inf. Model. 60 (2020) 5815–5831, https://doi.org/10.1021/acs.jcim.0c00575.
[48] B. Xia, X. Kang, Activation and maturation of SARS-CoV main protease, protein, Cell 2 (2011) 282–290, https://doi.org/10.1007/s13238-011-1034-1.
[49] N. Zhong, S. Zhang, P. Zou, J. Chen, X. Kang, Z. Li, C. Liang, C. Jin, B. Xia, Without its N-finger, the Main protease of severe acute respiratory syndrome coronavirus can form a novel dimer through its C-terminal domain, J. Virol. 82 (2008) 4227–4234, https://doi.org/10.1128/JVI.02612-07.
[50] P. Wei, K. Fan, H. Chen, L. Ma, C. Huang, L. Tan, D. Xi, C. Li, Y. Liu, A. Cao, L. Lai, The N-terminal octapeptide acts as a dimerization inhibitor of SARS coronavirus 3C-like proteinase, Biochem. Biophys. Res. Commun. 339 (2006) 865–872, https://doi.org/10.1016/j.bbrc.2005.11.102.
[51] J.C. Ferreira, S. Fadl, W.M. Rabeh, Key dimer interface residues impact the catalytic activity of 3CLpro, the main protease of SARS-CoV-2, J. Biol. Chem. 298 (2022) 102023, https://doi.org/10.1016/j.jbc.2022.102023.
[52] C.-Y. Chou, H.-C. Chang, W.-C. Hsu, T.-Z. Lin, C.-H. Lin, G.-G. Chang, Quaternary structure of the severe acute respiratory syndrome (SARS) coronavirus Main protease, Biochemistry 43 (2004) 14958–14970, https://doi.org/10.1021/bi0490237.
[53] G.D. Noske, Y. Song, R.S. Fernandes, R. Chalk, H. Elmassoudi, L. Koekemoer, C. D. Owen, T.J. El-Baba, C.V. Robinson, G. Oliva, A.S. Godoy, An in-solution snapshot of SARS-COV-2 main protease maturation process and inhibition, Nat. Commun. 14 (2023) 1545, https://doi.org/10.1038/s41467-023-37035-5.
[54] S. Mazzini, L. Musso, S. Dallavalle, R. Artali, Putative SARS-CoV-2 Mpro inhibitors from an in-house library of natural and nature-inspired products: a virtual screening and molecular docking study, Molecules 25 (2020) 3745, https://doi.org/10.3390/molecules25163745.
[55] A.E. Gorbalenya, E.J. Snijder, J. Ziebuhr, Virus-encoded proteinases and proteolytic processing in the Nidovirales, J. Gen. Virol. 81 (2000) 853–879, https://doi.org/10.1099/0022-1317-81-4-853.
[56] W.-C. Hsu, H.-C. Chang, C.-Y. Chou, P.-J. Tsai, P.-I. Lin, G.-G. Chang, Critical assessment of important regions in the subunit association and catalytic action of the severe acute respiratory syndrome coronavirus Main protease, J. Biol. Chem. 280 (2005) 22741–22748, https://doi.org/10.1074/jbc.M502556200.
[57] J. Shi, J. Sivaraman, J. Song, Mechanism for controlling the dimer-monomer switch and coupling dimerization to catalysis of the severe acute respiratory syndrome coronavirus 3C-like protease, J. Virol. 82 (2008) 4620–4629, https://doi.org/10.1128/JVI.02680-07.
[58] J. Barrila, U. Bacha, E. Freire, Long-range cooperative interactions modulate dimerization in SARS 3CL ^{pro}, Biochemistry 45 (2006) 14908–14916, https://doi.org/10.1021/bi0616302.
[59] P.-Y. Lin, C.-Y. Chou, H.-C. Chang, W.-C. Hsu, G.-G. Chang, Correlation between dissociation and catalysis of SARS-CoV main protease, Arch. Biochem. Biophys. 472 (2008) 34–42, https://doi.org/10.1016/j.abb.2008.01.023.
[60] L. Alzyoud, M.A. Ghattas, N. Atatreh, Allosteric binding sites of the SARS-CoV-2 Main protease: potential targets for broad-Spectrum anti-coronavirus agents, Drug Des. Devel. Ther. 16 (2022) 2463–2478, https://doi.org/10.2147/DDDT.S370574.
[61] T.J. El-Baba, C.A. Lutomski, A.L. Kantsadi, T.R. Malla, T. John, V. Mikhailov, J. R. Bolla, C.J. Schofield, N. Zitzmann, I. Vakonakis, C.V. Robinson, Allosteric inhibition of the SARS-CoV-2 Main protease: insights from mass spectrometry based assays**, Angew. Chem. Int. Ed. 59 (2020) 23544–23548, https://doi.org/10.1002/anie.202010316.
[62] J. Barrila, S.B. Gabelli, U. Bacha, L.M. Amzel, E. Freire, Mutation of Asn28 disrupts the dimerization and enzymatic activity of SARS 3CL ^{pro}, Biochemistry 49 (2010) 4308–4317, https://doi.org/10.1021/bi1002585.
[63] B.-L. Ho, S.-C. Cheng, L. Shi, T.-Y. Wang, K.-I. Ho, C.-Y. Chou, Critical assessment of the important residues involved in the dimerization and catalysis of MERS coronavirus Main protease, PloS One 10 (2015) e0144865, https://doi.org/10.1371/journal.pone.0144865.